

1



2

DOCTORAL THESIS

---

3

4      Optimisation studies and background  
5      estimation in searches for the supersymmetric  
6      partner of the top quark in all-hadronic final  
7      states with the ATLAS Detector at the LHC

---

8

9      *A thesis submitted in fulfillment of the requirements  
10     for the degree of Doctor of Philosophy*

11

*in the*

12

Experimental Particle Physics Research Group  
School of Mathematical and Physical Sciences

13

14

*Author:*

Fabrizio MIANO

*Supervisor:*

Dr. Fabrizio SALVATORE

15

20th October 2017

Dedicated to my family.

*Have no fear for atomic energy  
'cause none of them can stop the  
time*

17

---

Robert Nesta Marley

18

## *Acknowledgments*

- 19 Thanks to every single thing that went wrong. It made me stronger.

## *Declaration*

21 I, Fabrizio MIANO, hereby declare that this thesis, titled, "Optimisation studies and back-  
22 ground estimation in searches for the supersymmetric partner of the top quark in all-  
23 hadronic final states with the ATLAS Detector at the LHC" has not been and will not be,  
24 submitted in whole or in part to another University for the award of any other degree.

25 *Brighton, June 2018*

27

University of Sussex

28

School of Mathematical and Physical Sciences

29

Experimental Particle Physics Research Group

30

Doctoral Thesis

31

---

32    Optimisation studies and background estimation in searches for  
33    the supersymmetric partner of the top quark in all-hadronic final  
34    states with the ATLAS Detector at the LHC

---

35

36

by Fabrizio MIANO

37

## *Abstract*

38    This thesis presents searches for supersymmetry in  $\sqrt{s} = 13$  TeV proton-proton collisions  
39    at the LHC using data collected by the ATLAS detector in 2015, 2016 and 2017. Events  
40    with 4 or more jets and missing transverse energy were selected. Kinematic variables were  
41    investigated and optimisations were performed to increase the sensitivity to supersym-  
42    metric signals. Standard Model backgrounds were estimated by means of Monte Carlo  
43    simulations and data-driven techniques. Before analysing the data in the blinded signal  
44    regions the agreement between data and background predictions and the extrapolations  
45    from control and validation regions to signal regions were validated. The analysis yiel-  
46    ded no significant excess in any of the analyses performed. Therefore limits were set and  
47    the results were interpreted as lower bounds on the masses of supersymmetric particles  
48    in various scenarios and models.

# <sup>49</sup> Contents

<sup>50</sup>	<b>Introduction</b>	<b>1</b>
<sup>51</sup>	<b>1 The Standard Model, Supersymmetry, and the motivations behind it</b>	<b>2</b>
<sup>52</sup>	<b>1.1 Overview</b> . . . . .	2
<sup>53</sup>	<b>1.2 Limitations of the Standard Model</b> . . . . .	8
<sup>54</sup>	<b>1.3 Supersymmetry</b> . . . . .	11
<sup>55</sup>	<b>1.3.1 Why SUSY?</b> . . . . .	11
<sup>56</sup>	<b>1.3.2 SUSY Models</b> . . . . .	11
<sup>57</sup>	<b>1.3.3 Third generation Supersymmetry</b> . . . . .	12
<sup>58</sup>	<b>2 The ATLAS Experiment at the LHC</b>	<b>13</b>
<sup>59</sup>	<b>2.1 The LHC</b> . . . . .	13
<sup>60</sup>	<b>2.2 The ATLAS Detector</b> . . . . .	15
<sup>61</sup>	<b>2.2.1 The Magnet System</b> . . . . .	17
<sup>62</sup>	<b>2.2.2 The Inner Detector</b> . . . . .	18
<sup>63</sup>	<b>2.2.3 The Calorimeters</b> . . . . .	21
<sup>64</sup>	<b>2.2.4 The Muon Spectrometer</b> . . . . .	22
<sup>65</sup>	<b>2.3 The ATLAS Trigger System</b> . . . . .	23
<sup>66</sup>	<b>2.3.1 Level 1 Trigger</b> . . . . .	25
<sup>67</sup>	<b>2.3.2 High-Level Trigger</b> . . . . .	25
<sup>68</sup>	<b>3 The <i>b</i>-jet Trigger Signature in ATLAS</b>	<b>26</b>
<sup>69</sup>	<b>3.1 Trigger Efficiency</b> . . . . .	26
<sup>70</sup>	<b>4 Event Simulation and Reconstruction</b>	<b>27</b>
<sup>71</sup>	<b>4.1 Event Generation</b> . . . . .	27
<sup>72</sup>	<b>4.1.1 Parton Distribution Functions (PDFs)</b> . . . . .	27
<sup>73</sup>	<b>4.1.2 Matrix Element Calculation</b> . . . . .	27

74	4.1.3 Parton Showers . . . . .	27
75	4.1.4 Hadronisation . . . . .	27
76	4.2 Detector Simulation . . . . .	27
77	<b>5 Stop searches in final states with jets and missing transverse energy</b>	28
78	<b>6 Results and Statistical Intepretations</b>	29
79	<b>Trigger</b>	30
80	<b>Bibliography</b>	31

# **81 List of Tables**

82	1.1 Forces and mediators described by the SM . . . . .	5
----	--	---

# <sup>83</sup> List of Figures

<sup>84</sup> 1.1	The Higgs potential in the complex plane. . . . .	8
<sup>85</sup> 1.2	Summary of several Standard Model total production cross section measurements, corrected for leptonic branching fractions, compared to the corresponding theoretical expectations. All theoretical expectations were calculated at NLO or higher. The luminosity used for each measurement is indicated close to the data point. Uncertainties for the theoretical predictions are quoted from the original ATLAS papers. They were not always evaluated using the same prescriptions for PDFs and scales. Not all measurements are statistically significant yet [1]. . . . .	9
<sup>93</sup> 1.3	One-loop quantum corrections to the Higgs mass: (a) a fermion correction with coupling $\lambda_f$ and (b) a scalar correction with coupling $\lambda_S$ . . . . .	10
<sup>95</sup> 2.1	CERN Accelerator complex. The LHC is the last ring (dark grey line). Smaller machines are used for early-stage acceleration and also to provide beams for other experiments [2]. . . . .	15
<sup>98</sup> 2.2	Cut-away view of the ATLAS detector. The dimensions of the detector are 25 m in height and 44 m in length. The overall weight of the detector is approximately 7000 tonnes [2]. . . . .	16
<sup>101</sup> 2.3	The ATLAS magnet system. . . . .	17
<sup>102</sup> 2.4	The ATLAS Inner Detector . . . . .	19
<sup>103</sup> 2.5	A computer generated image of the full calorimeter. . . . .	21
<sup>104</sup> 2.6	Cut-away view of the ATLAS muon system [3]. . . . .	23
<sup>105</sup> 2.7	The ATLAS TDAQ system. L1Topo and FTK were being commissioned during 2015 and not used for the results shown in this thesis [4]. . . . .	24

# <sup>107</sup> Introduction

<sup>108</sup> Last thing to write

<sup>109</sup> **1** | <sup>110</sup> **The Standard Model, Supersym-**  
<sup>111</sup> **metry, and the motivations be-**  
<sup>112</sup> **hind it**

*A theory is something nobody believes, except the person who made it. An experiment is something everybody believes, except the person who made it.*

---

Albert Einstein

<sup>113</sup> The Standard Model (SM) of particle physics is an effective theory that aims to provide  
<sup>114</sup> a general description of fundamental particles and the phenomena we see in nature, i. e.  
<sup>115</sup> the way they interact. Unfortunately, our understanding of nature is still limited due to  
<sup>116</sup> some opened question to which the SM is not able to answer to, yet.

<sup>117</sup> In this chapter, an overview of the SM will be presented in Section 1.1 together with  
<sup>118</sup> the limitations of such theory and some of the reasons behind the need of an extension.  
<sup>119</sup> For the last decades theoretical physicsts have been trying to provide extensions to the  
<sup>120</sup> SM, the so-called beyond-the-SM theories. Among these, one of the most popular, Super-  
<sup>121</sup> symmetry which will be discussed in Section 1.3.

<sup>122</sup> **1.1 Overview**

<sup>123</sup> The 20<sup>th</sup> century can be considered a quantum revolution. Several experiments led to  
<sup>124</sup> discoveries which were found to be, together with the formalised theory, a solid base of  
<sup>125</sup> the Standard Model of particle physics and our description of nature. Several particles  
<sup>126</sup> were predicted first by the SM and then experimentally observed e. g. the  $W$  and the  $Z$

<sup>127</sup> bosons, the  $\tau$  lepton, [5], and more recently the Higgs boson at the LHC discovered by  
<sup>128</sup> ATLAS [6] and CMS [7].

<sup>129</sup> The SM lays on a Quantum Field Theory (QFT) where particles are treated like fields.  
<sup>130</sup> It can describe three of the four fundamental forces; weak, electromagnetic, and strong.  
<sup>131</sup> As of today, gravity is not considered in the SM. Sections 1.1 and 1.2 will be focused on  
<sup>132</sup> the description of the fields together with the carriers of the information, and on the lim-  
<sup>133</sup> itations that such theory implies, respectively.

<sup>134</sup> The most general classification of the particles within the SM can be made by means of  
<sup>135</sup> spin. Fermions have half-integer spin values - and are usually referred to as matter -, and  
<sup>136</sup> bosons have integer-spin values. A noteworthy subset of bosons is formed by the Spin-1  
<sup>137</sup> bosons (also known as gauge bosons). These can be considered the information carriers  
<sup>138</sup> or, in fact, the mediators of the forces.

### <sup>139</sup> Fermions

<sup>140</sup> Six quarks and six leptons belong to the fermions family. In particular, fermions can be  
<sup>141</sup> grouped into three generations. Each generation contains four particles; one up- and one  
<sup>142</sup> down-type quark, one charged lepton and one neutral lepton. The masses of the charged  
<sup>143</sup> leptons and quarks increase with the generation. The six quarks of the SM can be grouped  
<sup>144</sup> into three doublets:

$$\begin{pmatrix} u \\ d \end{pmatrix}, \quad \begin{pmatrix} c \\ s \end{pmatrix}, \quad \begin{pmatrix} t \\ b \end{pmatrix}$$

<sup>145</sup> The up-type quarks (up, charm, top) have charge  $+\frac{2}{3}e$  and the down-type quarks (down,  
<sup>146</sup> strange, beauty/bottom) have charge  $-\frac{1}{3}e$ , where  $e$  is the electron charge. Quarks also  
<sup>147</sup> have another quantum number that can be seen as the analogue of the electric charge,  
<sup>148</sup> which is the colour charge. This can exist in three different states; "red", "green" and  
<sup>149</sup> "blue". Moreover, as a consequence of *confinement*, which will be discussed later on in  
<sup>150</sup> this section, quarks cannot exist as free particles. They rather group to form hadronic  
<sup>151</sup> matter, also known as *hadrons*. There are two kinds of hadrons; mesons and baryons.  
<sup>152</sup> Mesons are quark-antiquark systems, e.g. the pion, and baryons are three-quark system,  
<sup>153</sup> e.g. protons and neutrons. Quarks and anti-quarks have a baryon number of  $\frac{1}{3}$  and  $-\frac{1}{3}$ ,  
<sup>154</sup> respectively.

<sup>155</sup> There are six leptons and they can be classified in charged leptons (electron  $e$ , muon  
<sup>156</sup>  $\mu$ , tau  $\tau$ ) and neutral leptons (electron neutrino  $\nu_e$ , muon neutrino  $\nu_\mu$ , tau neutrino  $\nu_\tau$ ).

$$\begin{pmatrix} \nu_e \\ e^- \end{pmatrix}, \quad \begin{pmatrix} \nu_\mu \\ \mu^- \end{pmatrix}, \quad \begin{pmatrix} \nu_\tau \\ \tau^- \end{pmatrix}$$

157 Each lepton has a characteristic quantum number, called lepton number ( $L$ ). Negatively  
158 (positively) charged leptons have  $L = -1$  ( $L = 1$ ) and neutral leptons have  $L = 0$ . The  
159 lepton number is conserved in all the interactions.

## 160 Forces of Nature

161 Forces in the SM are described by gauge theories, where the interactions is mediated by  
162 a vector gauge boson.

163 The electromagnetic force is described by Quantum ElectroDynamics (QED) and, as  
164 its mediator is the photon ( $\gamma$ ) which couples to charged particles, it only affects charged  
165 leptons and quarks, not neutrinos. They are instead affected by the weak force which is  
166 mediated by the bosons  $W^\pm$  and  $Z^0$ .

167 The weak interaction is associated with handedness (the projection of a particle spin  
168 onto its direction of motion). Both leptons and quarks have left- and right-handed com-  
169 ponents. However, only the left-handed (right-handed) component for neutrinos (anti-  
170 neutrinos) has been observed. This means that nature prefers to produce left-handed  
171 neutrinos and right-handed anti-neutrinos, which is the so-called parity violation.

172 The strong interactions, mediated by the gluon (electrically neutral and massless), is  
173 described by Quantum ChromoDynamics (QCD). Its coupling increases with increasing  
174 distance and is smaller at short range. Moreover, due to gluon self interactions, two  
175 different phenomena arise; *confinement*: neither quarks nor gluons are observed as free  
176 particles, but only colourless “singlet” states can be observed as “jets”, namely collim-  
177 ated cone-shaped sprays of hadrons; *asymptotic freedom*: interactions between quarks and  
178 gluons become weaker as the energy scale increases and the corresponding length scale  
179 decreases.

180 Table 1.1 summarises the forces described in the SM and their mediators’ main char-  
181 achteristics. Finally, the gravitational force, which is believed to be mediated by the grav-  
182 iton, is not included in Table 1.1 as it is not part of the SM.

## 183 Symmetries and Gauge Groups

184 In 1915, the mathematician Emmy Noether (23 March 1882 – 14 April 1935) proved that  
185 every differentiable symmetry of the action - defined as the integral over space of a Lag-

Table 1.1: Forces and mediators described by the SM

Force	Name	Symbol	Mass [GeV]	Charge
Electromagnetic	Photon	$\gamma$	0	0
Weak	W	$W^\pm$	80.398	$\pm e$
	Z	$Z^0$	91.188	0
Strong	Gluon	$g$	0	0

<sup>186</sup> rangian density function - of a physical system has a corresponding conservation law.  
<sup>187</sup> More generally, a symmetry is a property of a physical system. Under certain transform-  
<sup>188</sup> ations this property is preserved.

<sup>189</sup> A gauge theory in QFT, is a theory in which the Lagrangian is invariant under a con-  
<sup>190</sup> tinuous group of local transformation. Group theory was then adopted to describe the  
<sup>191</sup> symmetries conserved in the SM. The gauge group of the theory is the *Lie Group*. It con-  
<sup>192</sup> tains all the transformations between possible gauges. The Lie algebra of group generators  
<sup>193</sup> is therefore associated with any Lie group and for each group generator there emerges a  
<sup>194</sup> corresponding field: the gauge field. The quanta of the gauge fields are called *gauge bo-*  
<sup>195</sup> *sons*.

<sup>196</sup> The three SM interactions can therefore be mathematically described by the following:

$$U(1)_Y \otimes SU(2)_L \otimes SU(3)_C \quad (1.1)$$

<sup>197</sup> Here,  $Y$  is the weak hypercharge, used to estimate the correlation between the electric  
<sup>198</sup> charge ( $Q$ ) and the third component of the weak isospin ( $I_3$ ) via the relation  $Q = I_3 + Y/2$ ,  
<sup>199</sup> where  $I_3$  can either be  $\pm 1/2$  or 0 for left-handed and right-handed particles, respectively;  
<sup>200</sup>  $C$  the colour charge and  $L$  the left-handedness.

<sup>201</sup> As of today, we can describe three of the four forces of nature with group theory. QED  
<sup>202</sup> is an Abelian gauge theory with  $U(1)$  as symmetry group, with the electromagnetic four-  
<sup>203</sup> potential as its gauge field and with the photon as its gauge boson [8]. The interactions  
<sup>204</sup> between charged fermions occurs by the exchange of a massless photon.

<sup>205</sup> The weak interaction and the strong interactions are non-Abelian gauge theories with  
<sup>206</sup> gauge groups  $SU(2)$  and  $SU(3)$ , respectively. As a consequence of being non-Abelian  
<sup>207</sup> the generators commutators are non-vanishing and therefore the gauge bosons can self-  
<sup>208</sup> interact. The  $SU(2)$  generators of the weak interaction are the massless gauge bosons  
<sup>209</sup>  $W_\mu^{\alpha=1,\dots,3}$  and, as mentioned earlier on in this chapter, they violate the parity by acting  
<sup>210</sup> only on left-handed particles.

211 The gauge bosons of  $SU(3)_C$  are eight massless gluons,  $G_\mu^{\alpha=1,\dots,8}$ . The strong interaction  
 212 does not distinguish left- and right-handed particles. Finally, the Quarks that interact  
 213 through weak interaction are mixtures of SM eigenstates as described by the CKM matrix  
 214 [9].

## 215 Electroweak Symmetry Breaking and the Higgs mechanism

216 In 1979 Sheldon Glashow, Abdus Salam, and Steven Weinberg were awarded the Nobel  
 217 Prize in Physics for their contributions to the so-called electroweak unification. In  
 218 the mathematical description of the SM in 1.1 the electroweak interaction is described by  
 219  $U(1)_Y \otimes SU(2)_L$ . The electroweak physical bosons  $W$ ,  $Z$  and  $\gamma$  are related to the four  
 220 unphysical gauge bosons  $W_\mu^{\alpha=1,\dots,3}$  and  $B_\mu^0$ . In particular, to obtain the physical bosons  
 221 the gauge bosons have to mix as follows:

$$\begin{pmatrix} A_\mu \\ Z_\mu \end{pmatrix} = \begin{pmatrix} \cos \theta_W & \sin \theta_W \\ -\sin \theta_W & \cos \theta_W \end{pmatrix} \begin{pmatrix} B_\mu \\ W_\mu^3 \end{pmatrix} \quad (1.2)$$

222 Here,  $\theta_W$  is the so-called *Weinberg angle* which is the angle by which spontaneous sym-  
 223 metry breaking rotates the original  $W_\mu^3$  and  $B_\mu$ , producing the physical  $Z$ , and the photon.  
 224  $\theta_W$  can be experimentally determined in terms of the coupling strengths of the  $B_\mu(g_1)$  and  
 225 the  $W_\mu^\alpha(g_2)$  to the fermions using the relation  $\tan \theta_W = g_1/g_2$ . The field mixing of gauge  
 226 bosons that gives birth to the physical ones can be mathematically expressed by the fol-  
 227 lowing:

$$A_\mu = W_\mu^3 \sin \theta_W + B_\mu \cos \theta_W \quad (1.3)$$

228

$$Z_\mu = W_\mu^3 \cos \theta_W - B_\mu \sin \theta_W \quad (1.4)$$

229 where  $A_\mu$  and  $Z_\mu$  represent the photon and the  $Z$  boson, respectively. The charged vector  
 230 bosons,  $W_\mu^\mp$ , and its complex conjugate are defined as:

$$W_\mu^\pm = \frac{1}{\sqrt{2}} (W_\mu^1 \mp iW_\mu^2) \quad (1.5)$$

231 Mass terms for both gauge bosons and fermionic fields are not invariant under gauge  
 232 transformations and are therefore forbidden by the electroweak gauge. Nonetheless, it is  
 233 proven by experiments that  $W$  and  $Z$  are massive [8], therefore the SM assumption only  
 234 holds if the electroweak symmetry is broken.

<sup>235</sup> The SM Lagrangian can be written as the sum of the various Lagrangians describing  
<sup>236</sup> the three interactions and the masses of the elementary particles as follows:

$$\mathcal{L}_{\text{SM}} = \mathcal{L}_{\text{EWK}} + \mathcal{L}_{\text{QCD}} + \mathcal{L}_{\text{Mass}} \quad (1.6)$$

<sup>237</sup> In order for the SM Lagrangian to remain a renormalisable theory, mass terms ( $\mathcal{L}_{\text{Mass}}$ )  
<sup>238</sup> cannot be inserted by hand. A mechanism, that can preserve the gauge symmetry in  
<sup>239</sup> the SM and, that can solve the inconsistency arisen from the mass difference between  
<sup>240</sup> the gauge bosons and the physical ones, is needed. A British theoretical physicist, Peter  
<sup>241</sup> Higgs (29 May 1929, Newcastle upon Tyne, UK), came up with a brilliant solution for  
<sup>242</sup> which he was awarded the 2013 Physics Nobel Prize. In the 1960s, Higgs proposed that  
<sup>243</sup> broken symmetry in electroweak theory could explain the origin of masses of elementary  
<sup>244</sup> particles, and in particular of  $W$  and  $Z$  bosons: the Higgs mechanism was given birth.  
<sup>245</sup> The mechanism introduces a scalar field, known as the Higgs field, thought to couple to  
<sup>246</sup> both massive fermions and bosons.

<sup>247</sup> In the SM the Higgs field is a doublet in  $SU(2)$ :

$$\phi = \begin{pmatrix} \phi^+ \\ \phi^0 \end{pmatrix} \quad (1.7)$$

<sup>248</sup> with  $\phi^+$  and  $\phi^0$  being generic complex fields:

$$\phi^+ = \frac{\phi_1 + i\phi_2}{\sqrt{2}}, \quad \phi^0 = \frac{\phi_3 + i\phi_4}{\sqrt{2}} \quad (1.8)$$

<sup>249</sup> Consider a Lagrangian of the form:

$$\mathcal{L}_{\text{Higgs}} = (\partial_\mu \phi)^* (\partial^\mu \phi) - V(\phi) \quad (1.9)$$

<sup>250</sup> Renormalizability and  $SU(2)_L \otimes U(1)_Y$  invariance require the Higgs potential to be of the  
<sup>251</sup> following form:

$$V(\phi) = \mu^2 \phi^\dagger \phi + \lambda (\phi^\dagger \phi)^2 \quad (1.10)$$

<sup>252</sup> Eq. 1.9 is the Higgs Lagrangian if  $\phi$  is chosen to be the following:

$$\phi = \begin{pmatrix} \phi^+ \\ \phi^0 \end{pmatrix} = \begin{pmatrix} G^+ \\ \frac{1}{\sqrt{2}} (v + H + iG^0) \end{pmatrix}$$

253 Here, the complex scalar field  $G^\pm$  and the real scalar field  $G^0$  correspond to Goldstone  
 254 bosons, and the real scalar field  $H$  is the SM Higgs boson field [10]. These massless scalars  
 255 are absorbed due to the gauge transformations by the electroweak gauge bosons of the SM:

$$\phi = \begin{pmatrix} \phi^+ \\ \phi^0 \end{pmatrix} = \begin{pmatrix} 0 \\ \frac{1}{\sqrt{2}}(v + H) \end{pmatrix} \quad (1.11)$$

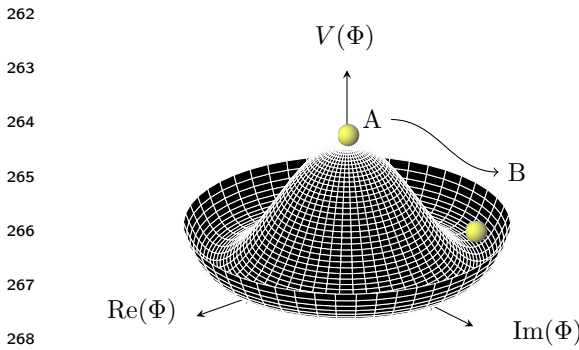
256 The Higgs potential in Eq. 1.10 is displayed in Fig. 1.1 if  $\lambda$  and  $\mu$  are chosen to be  
 257 real. Such potential has a non-zero ground state,  $v$ , also known as *vacuum expectation*  
 258 *value* (VEV):

$$\phi_0 = \begin{pmatrix} 0 \\ \frac{1}{\sqrt{2}}v \end{pmatrix} \quad (1.12)$$

259 Such representation remains invariant under  $U(1)$  allowing electric charge conservation.  
 260 However, the SM gauge symmetry 1.1 is broken into  $SU(2)_L \otimes U(1)_Y$ .

261

In summary, to generate particle masses  
 gauge symmetry must be broken. However, in order for the theory to remain  
 renormalisable, the global Lagrangian  
 symmetry must be preserved. This can be  
 solved introducing the concept of *spontaneous*  
*symmetry breaking* (SSB): a mechanism  
 that allows a symmetric Lagrangian,  
 but not a symmetric VEV. In particular,



270 Figure 1.1: The Higgs potential in the complex plane.

271 given a Lagrangian invariant under a cer-  
 tain transformation,  $T_X$  and a generic set  
 272 of states, that transform under  $T_X$  as the elements of a multiplet, the symmetry is spon-  
 273 taneously broken if one of those states is arbitrarily chosen as the ground state of the sys-  
 274 tem. The interaction of the Higgs field with the  $SU(2) \otimes U(1)$  gauge fields,  $W_\mu^\alpha = 1, 2, 3$ ,  
 275 result in the three gauge bosons fields acquiring mass whilst the  $B_0$  field stays massless.

## 276 1.2 Limitations of the Standard Model

277 During Run 1 and 2 of the LHC, the SM has been extensively validated, as shown in Fig.  
 278 1.2: the agreement, between the measured production cross section of various SM pro-  
 279 cesses and the SM predictions, looks very good. However, the reasons behind the mass

difference between the three generations of fermions are still not explained by the SM because masses are treated as free parameters of the theory. In addition, there are some fundamental questions that have still no answer and they will be briefly discussed this section.

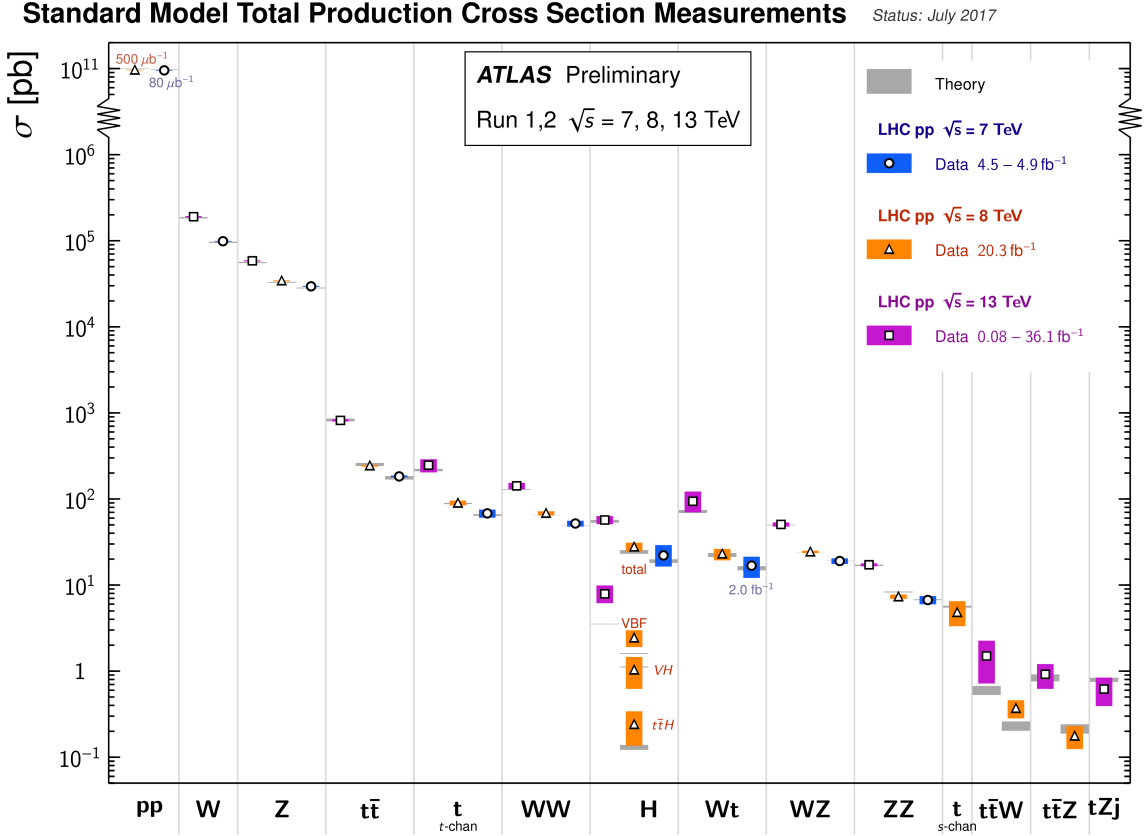


Figure 1.2: Summary of several Standard Model total production cross section measurements, corrected for leptonic branching fractions, compared to the corresponding theoretical expectations. All theoretical expectations were calculated at NLO or higher. The luminosity used for each measurement is indicated close to the data point. Uncertainties for the theoretical predictions are quoted from the original ATLAS papers. They were not always evaluated using the same prescriptions for PDFs and scales. Not all measurements are statistically significant yet [1].

## 284 Hierarchy Problem

285 Due to the coupling of every particle to the Higgs field, the one-loop corrections to the  
286 Higgs mass receive several contributions.

287 In particular, as shown in Fig. 1.3:

$$\Delta m_H^2 = -\frac{|\lambda_f|^2}{8\pi^2} \Lambda_{UV}^2 + \dots \quad (1.13)$$

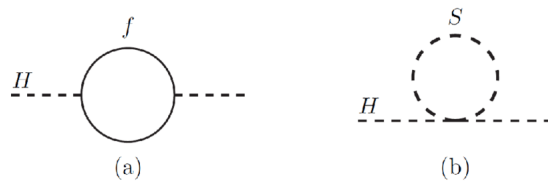


Figure 1.3: One-loop quantum corrections to the Higgs mass: (a) a fermion correction with coupling  $\lambda_f$  and (b) a scalar correction with coupling  $\lambda_S$ .

288 which is the dominant, due to the fermionic contribution, and

$$\Delta m_H^2 = -\frac{|\lambda_S|^2}{16\pi^2} \left[ \Lambda_{UV}^2 - 2m_S^2 \ln(\Lambda_{UV}/m_S) + \dots \right] \quad (1.14)$$

289 due to the bosonic contribution. Here,  $\lambda_f$  and  $\lambda_S$  are the coupling to the fermionic field  
290 and the scalar field, respectively;  $\Delta m_H^2$  is the difference between the observed Higgs mass  
291  $m_H^2$  and the bare mass,  $m_H^0$  (Lagrangian parameter);  $\Lambda_{UV}$  is the ultraviolet momentum  
292 cut-off, selected to be at the Planck scale ( $\sim 2 \cdot 10^{18}$  GeV), at which a QFT description  
293 of gravity is believed to become possible. The correction to the Higgs mass then, will  
294 be around 30 orders of magnitude larger than Higgs mass itself, in opposition to what  
295 has been measured. This difference just mentioned, between the electroweak scale and  
296 the Planck scale arisen from the quantum corrections to the Higgs mass, is the so-called  
297 Hierarchy Problem [11].

## 298 Neutrino Masses

299 The Super-Kamiokande Collaboration first, in 1998 [12], and SNO Collaboration later, in  
300 2001 [13], have provided measurements of the neutrino flux from solar and atmospheric  
301 sources. The Nobel Prize in Physics 2015 was awarded jointly to Takaaki Kajita and Arthur  
302 B. McDonald “for the discovery of neutrino oscillations, which shows that neutrinos have  
303 mass” [14]. Such feature contradicts the absence of a mechanism for mass generation for  
304 the neutrinos.

305 Various exotic solutions are on the market: one possible solution could be to add the  
306 so-called Majorana mass terms for the neutrino (seesaw mechanism). Neutrino physics  
307 could unveil physics beyond the SM.

## 308 Dark Matter

309 Although dark matter (DM) has never been directly observed, its existence is inferred  
310 from its gravitational effects. For example, looking at galaxies rotation, it was observed  
311 that the rotation speed was higher than expected, given the amount of visible matter. Two

<sup>312</sup> different reasoning arose during the last century to justify such effect either there is matter  
<sup>313</sup> that cannot be seen by us (in terms of visible light), which contributes to the galactic mass;  
<sup>314</sup> or the general relativity works differently at galactic distances. The former is believed to  
<sup>315</sup> be the most likely and it implies the existence of new particles which do not interact via  
<sup>316</sup> electromagnetic interaction, the so-called Weakly Interacting Massive Particles (WIMPs).

### <sup>317</sup> 1.3 Supersymmetry

<sup>318</sup> Supersymmetry links gravity with the other fundamental forces of nature by introducing  
<sup>319</sup> a space-time symmetry that relates bosons to fermions and vice-versa, via a transforma-  
<sup>320</sup> tion of the form of:

$$Q |\text{fermion}\rangle = |\text{boson}\rangle, \quad Q |\text{boson}\rangle = |\text{fermion}\rangle \quad (1.15)$$

<sup>321</sup> For each SM particle there exists a superpartner with a spin difference of  $\Delta s = 1/2$ . As of  
<sup>322</sup> today, superpartners, generally called *sparticles* (where the *s* stands for “scalar”), have not  
<sup>323</sup> been observed yet, resulting in the assumption that SUSY must be a broken symmetry,  
<sup>324</sup> otherwise superpartners would have the same quantum numbers and masses as their  
<sup>325</sup> SM equivalent. However, if sparticles were to be too heavy (close to the Planck scale),  
<sup>326</sup> the hierarchy problem would still remain unsolved. The *soft* SUSY breaking mechanism  
<sup>327</sup> overcomes this problem imposing contrains on the masses of sparticles to a range that can  
<sup>328</sup> be experimentally explored.

<sup>329</sup> In this section an overview of Supersymmetry (SUSY) will be presented, together with  
<sup>330</sup> the motivations behind the success of such theory. Third generation SUSY will be also dis-  
<sup>331</sup> cussed as it is the most relevant theoretical support to the analyses presented in Chapter  
<sup>332</sup> 5.

#### <sup>333</sup> 1.3.1 Why SUSY?

#### <sup>334</sup> 1.3.2 SUSY Models

#### <sup>335</sup> Minimal Supersymmetric Standard Model

<sup>336</sup> bla

#### <sup>337</sup> R-parity SUSY

<sup>338</sup> bla

<sup>339</sup> **Simplified models**

<sup>340</sup> bla

<sup>341</sup> **Phenomenological MSSM**

<sup>342</sup> bla

<sup>343</sup> **1.3.3 Third generation Supersymmetry**

## <sup>344</sup> 2 | The ATLAS Experiment at the <sup>345</sup> LHC

<sup>346</sup> ATLAS (A Toroidal LHC ApparatuS) is one of the four main experiments (ATLAS, CMS,  
<sup>347</sup> ALICE, LHCb) taking data at a center-of-mass energy of 13 TeV using beams delivered by  
<sup>348</sup> the Large Hadron Collider (LHC). In this chapter an overview of the LHC will be given  
<sup>349</sup> in Section 2.1, then the ATLAS detector will be described in Section 2.2, and finally the  
<sup>350</sup> Trigger system, used to cleverly store the data, will be described in Section 2.3. A more  
<sup>351</sup> in-depth description of the Trigger algorithms I have been involved in will be given in  
<sup>352</sup> Chapter 3.

### <sup>353</sup> 2.1 The LHC

<sup>354</sup> As of today, the LHC is the world's largest and most powerful particle accelerator. It was  
<sup>355</sup> designed to help answer some of the fundamental open questions in particle physics by  
<sup>356</sup> colliding protons at an unprecedented energy and luminosity. It is located at the European  
<sup>357</sup> Organisation for Nuclear Research (CERN), in the Geneva area, at a depth ranging from  
<sup>358</sup> 50 to 175 metres underground. It consists of a 27-kilometre ring made of superconducting  
<sup>359</sup> magnets, and inside it two high-energy particle beams travel in opposite directions and  
<sup>360</sup> in separate beam pipes.

<sup>361</sup> The beams are guided around the ring by a strong magnetic field generated by coils -  
<sup>362</sup> made of special electric cables - that can operate in a superconducting regime. 1232 super-  
<sup>363</sup> conducting dipole and 392 quadrupole magnets, with an average magnetic field of 8.3 T,  
<sup>364</sup> are employed and kept at a temperature below 1.7 K, in order to preserve their supercon-  
<sup>365</sup> ducting properties. The formers are used to bend the beams and the latters to keep them  
<sup>366</sup> focused while they get accelerated.

<sup>367</sup> The collider first went live on September 2008 even though, due to a magnet quench  
<sup>368</sup> incident that damaged over 50 superconducting magnets, it has been operational since

<sup>369</sup> November 2009 when low-energy beams circulated in the tunnel for the first time since the  
<sup>370</sup> incident. This also marked the start of the main research programme and the beginning  
<sup>371</sup> of the so-called Run 1: first operational run (2009 - 2013).

### <sup>372</sup> Performance of the LHC

<sup>373</sup> In June 2015 the LHC restarted delivering physics data, after a two-year break, the so-  
<sup>374</sup> called Long Shutdown 1 (LS1), during which the magnets were upgraded to handle the  
<sup>375</sup> current required to circulate 7-TeV beams. It was the beginning of the so-called Run 2 -  
<sup>376</sup> second operational run (2015-2018) - during which LHC has collided up to  $10^{11}$  bunches  
<sup>377</sup> of protons every 25 ns at the design luminosity - the highest luminosity the detector was  
<sup>378</sup> designed to cope with - of  $2 \cdot 10^{34} \text{ cm}^{-2} \text{s}^{-1}$ . The definition of the luminosity is:

$$\mathcal{L} = f \frac{n_b N_1 N_2}{4\pi\sigma_x\sigma_y} \quad (2.1)$$

<sup>379</sup> where  $N_1$  and  $N_2$  are the number of protons per bunch in each of the colliding beams,  $f$   
<sup>380</sup> is the revolution frequency of the bunch collisions,  $n_b$  the number of proton per bunch,  
<sup>381</sup> and  $\sigma_x$  and  $\sigma_y$  are the horizontal and vertical dimensions of the beam. The luminosity is  
<sup>382</sup> strictly related to the number of collisions occurring during a certain experiment via the  
<sup>383</sup> following:

$$\mathcal{N}_{\text{event}} = \mathcal{L}\sigma_{\text{event}} \quad (2.2)$$

<sup>384</sup> where  $\sigma_{\text{event}}$  is the cross section of the process under investigation. It has not only collided  
<sup>385</sup> protons but also heavy ions, in particular lead nuclei at  $\sqrt{s_{NN}} = 5.02 \text{ TeV}$ , at a luminosity  
<sup>386</sup> of  $10^{27} \text{ cm}^{-2} \text{s}^{-1}$  [15].

### <sup>387</sup> Acceleration stages

<sup>388</sup> Before reaching the maximum energy, the proton beams are accelerated by smaller ac-  
<sup>389</sup> celerators through various stages. Figure 2.1 shows a sketch of the CERN's accelerator  
<sup>390</sup> complex. It all begins at the linear accelerator LINAC 2. Here protons are accelerated up  
<sup>391</sup> to 50 MeV, and then injected in the Proton Synchrotron Booster (PSB) where they reach  
<sup>392</sup> 1.4 GeV. The next stage is the Proton Synchrotron (PS), which boosts the beams up to 25  
<sup>393</sup> GeV and then the Super Proton Synchrotron (SPS) makes them reach energies up to 450  
<sup>394</sup> GeV. Eventually, the beams are injected in bunches with a 25 ns spacing into the LHC,  
<sup>395</sup> where they travel in opposite directions, while they are accelerated to up to 13 TeV. Once

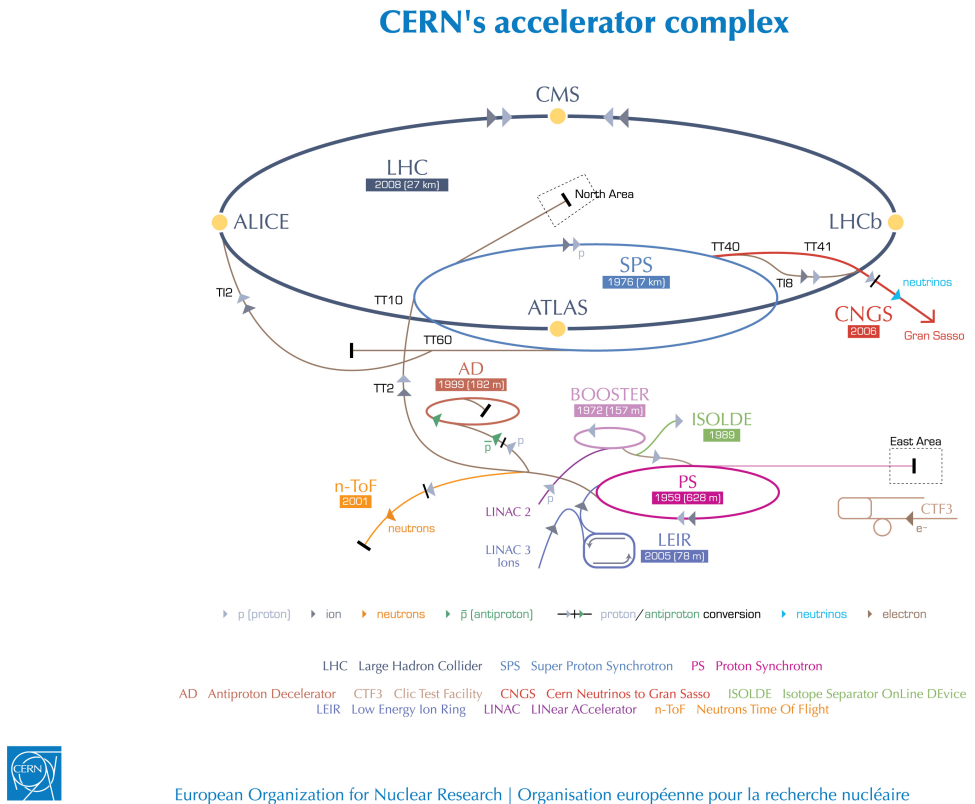


Figure 2.1: CERN Accelerator complex. The LHC is the last ring (dark grey line). Smaller machines are used for early-stage acceleration and also to provide beams for other experiments [2].

396 the bunches reach the maximum energy, they are made collide at four different points,  
 397 inside four experiments around the ring [16].

398 The heavy ion beams acceleration procedure is slightly different. Their journey starts  
 399 at LINAC 3 first, and the Low Energy Ion Ring (LEIR) then, before they make their way  
 400 into the PS where they follow the same path as the protons [16].

401 The four large detectors on the collision points are; the multi-purpose detectors A Tor-  
 402 oidal LHC ApparatuS (ATLAS), and Compact Muon Solenoid (CMS) [17], Large Hadron  
 403 Collider beauty (LHCb) [18], which focuses on flavour physics, and A Large Ion Collider  
 404 Experiment (ALICE) [19] which specialises in heavy ion physics. The *big four* are not the  
 405 only experiments at the CERN’s accelerator complex. There also are smaller experiments  
 406 based at the the four caverns about the collision points e.g. TOTEM, LHCf and MoEDAL,  
 407 but this will not be discussed any further in this thesis.

## 408 2.2 The ATLAS Detector

409 ATLAS is a general-purpose detector designed to collect data with the highest luminosity  
 410 provided by the LHC. It is located at CERN’s Point 1 cavern and it measures about 45 m in

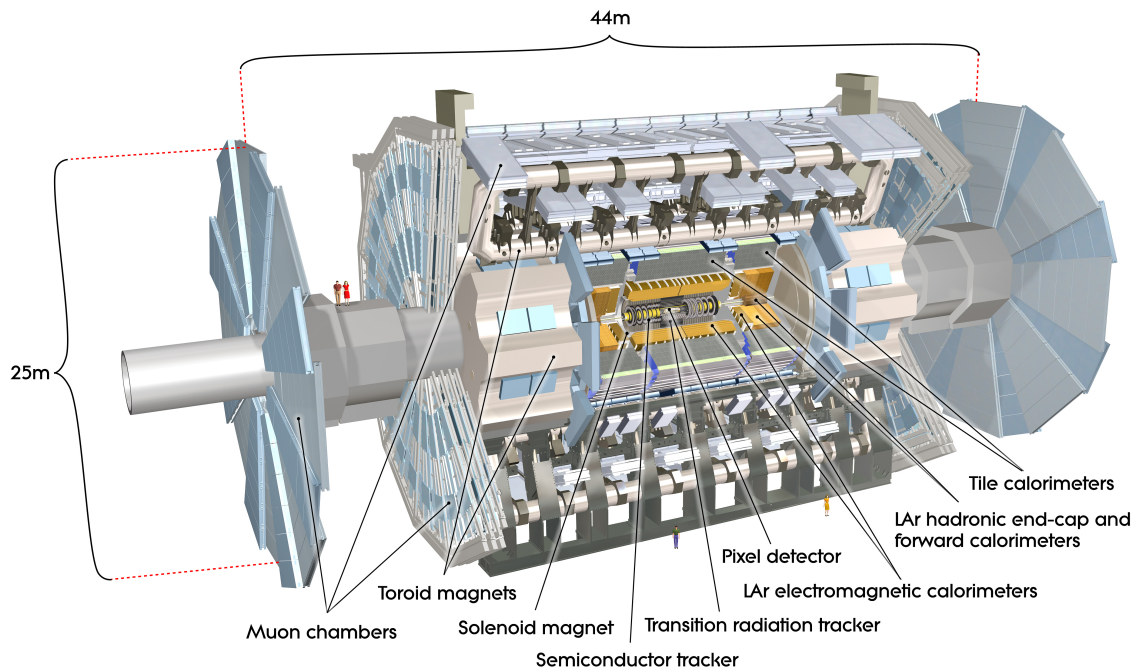


Figure 2.2: Cut-away view of the ATLAS detector. The dimensions of the detector are 25 m in height and 44 m in length. The overall weight of the detector is approximately 7000 tonnes [2].

length and 25 m in diameter. It has a forward-backward symmetric cylindrical geometry with respect to the interaction point and it is designed to reconstruct and measure physics objects such as electrons, muons, photons and hadronic jets. Its design was optimised to be as sensitive as possible to the discovery of the Higgs boson and beyond-the-Standard-Model (BSM) physics. In fact, thanks to the other sub-systems, ATLAS is able to observe all possible decay products by covering nearly  $4\pi$  steradians of solid angle.

In Figure 2.2 a cut-away view of ATLAS with all its components is shown. The inner-most layer is the Inner Detector (ID) which is the core of the tracking system and consists of a Pixel, a Silicon micro-strip tracker (SCT), and a Transition Radiation Tracker (TRT). It is submerged in a 2 T magnetic field, generated by a thin superconducting solenoid, which bends all the charged particles' trajectories allowing transverse momentum measurement. The electromagnetic and hadronic calorimeters form the next layer and they are both used to perform precise energy measurements of photons, electrons, and hadronic jets. Finally, the outermost layer corresponds to the Muon Spectrometer (MS) which, together with the ID, enclosed in a toroidal magnetic field, allows precise measurement of momentum and position of muons. These sub-detectors will be discussed in more detail in the following sections.

## 428 The ATLAS coordinate system

429 A coordinate system is taken on for the spatial definition of the sub-systems and kinematic  
 430 measurement of physics processes. Such system is defined starting from the interaction  
 431 point, defined as the origin. The  $z$ -axis is defined by the beam direction and the  $x - y$   
 432 plan, as transverse to the beam direction.

433 A quantity, known as pseudorapidity, ( $\eta$ ), is defined to describe the angle of a particle  
 434 coming out of the collision, with respect to the beam axis:

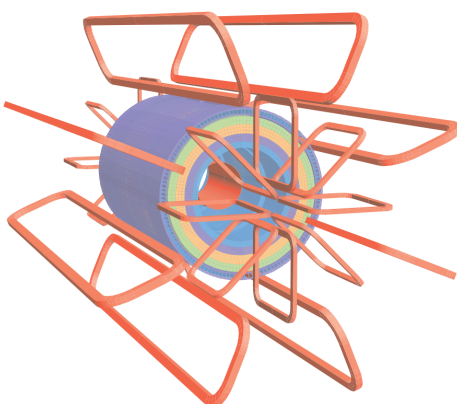
$$\eta \equiv -\ln(\tan(\theta/2))$$

435 Here  $\theta$  is the polar angle. The azimuthal angle,  $\phi$ , is defined around the beam axis and  
 436 the polar angle. In the  $(\eta, \phi)$  space a distance  $\Delta R$  can be therefore defined as

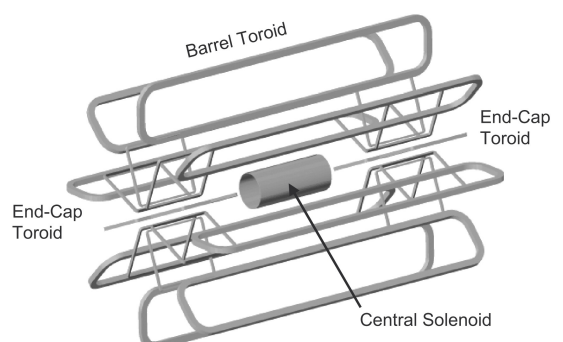
$$\Delta R = \sqrt{\Delta\eta^2 + \Delta\phi^2}$$

437 where  $\Delta\eta$  and  $\Delta\phi$  are the differences in pseudorapidity and azimuthal angle between any  
 438 two considered objects. A central and a forward region of pseudorapidity are also defined  
 439 such that the detector components are described as part of the *barrel* if they belong to the  
 440 former or as part of the *end-caps* if they belong to the latter.

### 441 2.2.1 The Magnet System



(a) Geometry of magnet windings and tile calorimeter steel. The eight barrel toroid coils, with the end-cap coils interleaved are visible. The solenoid winding lies inside the calorimeter volume [3].



(b) Schematic view of the superconducting magnets [20].

Figure 2.3: The ATLAS magnet system.

442 The ATLAS magnet system, 26 m long with a 22 m diameter, generates the magnetic field  
443 needed to bend the trajectories of charged particles in order to perform momentum meas-  
444 urement. Figure 2.3a and 2.3b show the geometry of the system and its components,  
445 which are made of NbTi - superconducting material - and will be described in the follow-  
446 ing paragraphs.

#### 447 **The Central Solenoid**

448 With an axial length of 5.8 m, an inner radius of 2.46 m, and an outer radius of 2.56 m, the  
449 central solenoid magnet is located between the ID and the ECAL. Its function is to bend  
450 the charged particles that go through the ID and it is aligned on the beam axis providing  
451 a 2 T axial magnetic field that allows accurate momentum measurement up to 100 GeV  
452 [20].

#### 453 **The Barrel and the End-cap Toroids**

454 Figure 2.3b displays the toroid magnetic system that surrounds the calorimeters. With its  
455 cylindrical shape this component consists of a barrel and two end-caps toroids, each with  
456 eight superconducting coils. The system allows accurate measurement of muon momenta  
457 using a magnetic field of approximately 0.5 T (barrel) for the central regions and 1 T (end-  
458 cap) for the end-cap regions, respectively, which bends the particles in the  $\theta$  direction.

#### 459 **2.2.2 The Inner Detector**

460 The Inner Detector (ID) [21] is the innermost component of the ATLAS detector i. e. the  
461 nearest sub-detector to the interaction region and it is used to reconstruct charged particle  
462 tracks used in the selection of physics objects. In fact, it allows robust track reconstruction,  
463 with accurate impact parameter resolution ( $\sim 20\mu m$ ) and precise primary and secondary  
464 vertex reconstruction for charged particles (tracks) above 500 MeV and within  $|\eta| < 2.5$ .

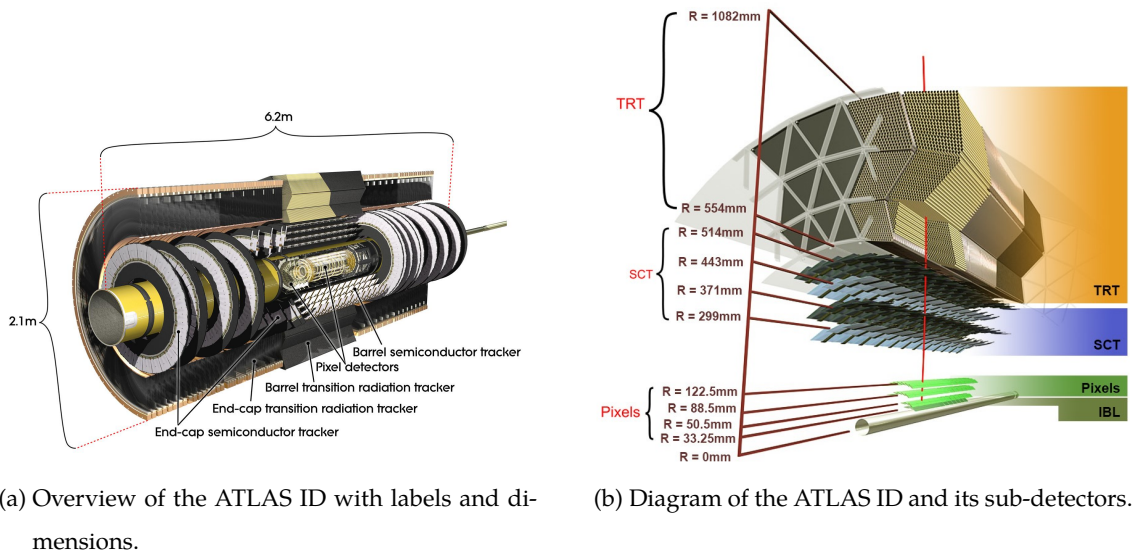
465 The ID is comprised of independent and concentric sub-systems, which are all shown  
466 in Figure 2.4:

- 467 • Insertable B-Layer (IBL):

468 innermost Pixel Detector layer added during ATLAS Run 2 upgrade (2013/2014) to  
469 improve vertexing and impact parameter reconstruction;

- 470 • Silicon Pixel Tracker (Pixel):

471 made of silicon pixel layers and used mainly for reconstructing both the primary



(a) Overview of the ATLAS ID with labels and dimensions.

(b) Diagram of the ATLAS ID and its sub-detectors.

Figure 2.4: The ATLAS Inner Detector

472 and secondary vertices in an event;

473 • SemiConductor Tracker (SCT):

474 comprised of silicon microstrip layers; thanks to its resolution ( $17 \times 580 \mu\text{m}$ ) it can  
475 accurately measure particle momenta;

476 • Transition Radiation Tracker (TRT):

477 final layer comprised of various layers of gaseous straw tube elements surrounded  
478 by transition radiation material.

479 These sub-detectors will be discussed in the following sections.

480 **IBL**

481 The IBL [22] is the innermost Pixel Detector layer as shown in Figure 2.4b. It is comprised  
482 of 6M channels and each pixel measures  $50 \times 250 \mu\text{m}$ . Its resolution is  $8 \times 40 \mu\text{m}$ ,  
483 The addition of this new layer brought a considerable improvement on the performance of the  
484 Pixel Detector by enhancing the quality of impact parameter reconstruction of tracks. In  
485 particular, this was achieved by improving the vertex finding efficiency and the tagging  
486 of bottom-quark-initiated jets ( $b$ -jets) which, in case of a B-layer failure, can be restored  
487 by the IBL. Besides these improvements, the IBL insertion allowed ATLAS to better cope  
488 with high luminosity effects such as the increase in event pile-up, which leads to high  
489 occupancy and read-out inefficiency.

---

## 490 Pixel

491 The Pixel detector is comprised of 1750 identical sensorchip-hybrid modules, each cover-  
 492 ing an active area of  $16.4 \times 60.8$  mm. The total number of modules correspond to roughly  
 493 80 million semiconductor silicon pixels. The nominal pixel size is  $50 \mu\text{m}$  in the  $\phi$  direction  
 494 and  $400 \mu\text{m}$  in the barrel region, along the  $z$ -axis (beam axis) [23]. The reason why such a  
 495 large amount of pixels is employed is justified by the need to cope with the high luminos-  
 496 ity in ATLAS. The silicon pixel detector measures 48.4 cm in diameter and 6.2 m in length  
 497 providing a pseudorapidity coverage of  $|\eta| < 2.5$ . Figure 2.4b shows the three concentric  
 498 barrel layers placed at 50.5 mm, 88.5 mm and 122.5 mm respectively. Furthermore, the  
 499 Pixel detector is made of six disk layers, three for each forward region, such that when a  
 500 charged particle crosses the layers it will generate a signal at least in three space points.  
 501 The fine granularity of such detector allows accurate measurement and precise vertex re-  
 502 construction, as it provides a more accurate position measurement as a large detection  
 503 area is available. In particular, it has a resolution of  $10 \times 115 \mu\text{m}$ .

## 504 SCT

505 The SCT is made of 4088 modules of silicon micro-strip detectors arranged in four con-  
 506 centric barrel layers. It is mainly used for precise momentum reconstruction over a range  
 507  $|\eta| < 2.5$  and it was designed for precision measurement of the position using four points  
 508 (corresponding to eight silicon layers), obtained as track hits when crossing the layers.  
 509 Figure 2.4b shows the structure of the SCT with its four concentric barrel layers with radii  
 510 ranging from 299 mm to 514 mm and two end-cap layers. Each module has an intrinsic  
 511 resolution of  $17 \mu\text{m}$  in the  $R - \phi$  direction and  $580 \mu\text{m}$  in the  $z$  direction. As the SCT is fur-  
 512 ther away from the beam-pipe than the Pixel detector, it has to cope with reduced particle  
 513 density. This allows for reduced granularity maintaining the same level of performance of  
 514 the Pixel detector: SCT can use  $\sim 6.3$  million read-out channels.

## 515 TRT

516 The last and outermost of the sub-systems in the ID is the TRT. It is a gaseous detector  
 517 which consists of 4 mm diameter straw tubes wound from a multilayer film reinforced  
 518 with carbon fibers and containing a  $30 \mu\text{m}$  gold plated tungsten wire in the center. The  
 519 straw is filled with a gas mixture of 70% Xe, 27% CO<sub>2</sub> and 3% O<sub>2</sub> [24]. As shown in Figure  
 520 2.4b, its section consists of three concentric layers with radii ranging from 544 mm to 1082  
 521 mm, each of which has 32 modules containing approximately 50,000 straws, 1.44 m in

---

length, aligned parallel to the beam direction with independent read-out at both ends.  
 Both end-cap sections are divided into 14 wheels, with roughly 320,000 straws in the R-direction. The average 36 hits per track in the central region of the TRT allow continuous tracking to enhance pattern recognition and momentum resolution in the  $|\eta| < 2.5$  region.  
 It also improves the  $p_T$  resolution for longer tracks.

### 2.2.3 The Calorimeters

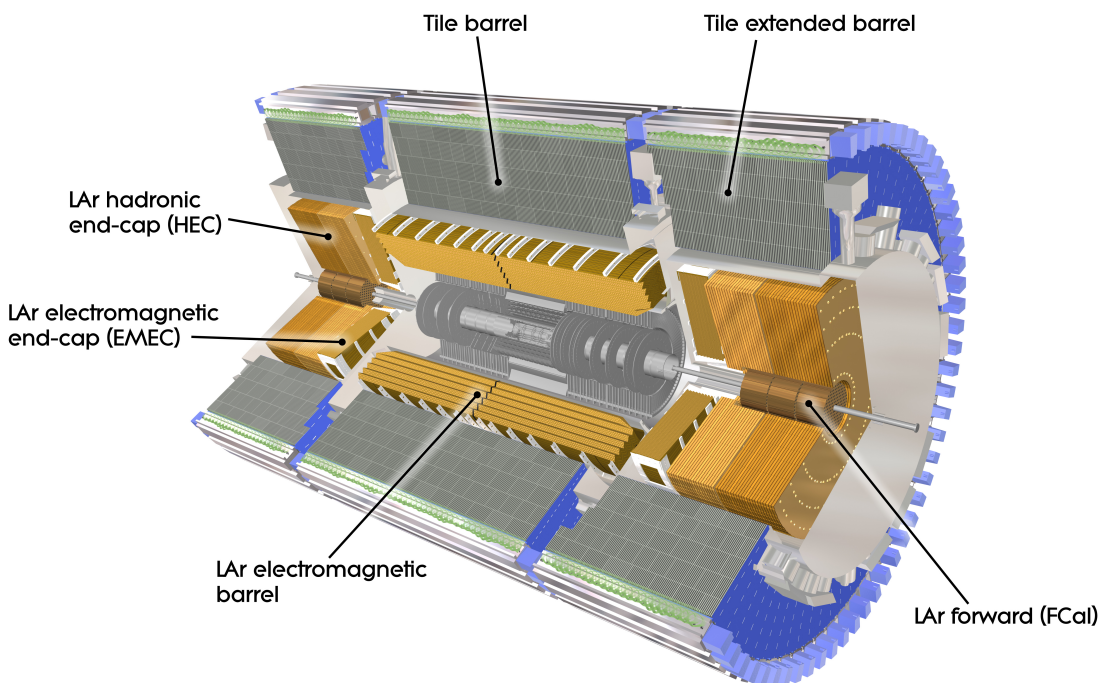


Figure 2.5: A computer generated image of the full calorimeter.

The ATLAS Calorimeter system, shown in Figure 2.5, is comprised of two main subsystems; the electromagnetic calorimeter (ECAL) and hadronic calorimeter (HCAL), which are designed to stop and measure the energy of electromagnetic-interacting and hadronic particles respectively. The combination of the two provides full coverage in  $\phi$  and  $|\eta| < 4.95$ . Particles slow down and lose energy generating showers when crossing different layers. The ECAL is comprised of one barrel and two end-cap sectors employing liquid Argon (LAr). The showers hereby develop as electrons pairs which are then collected. The HCAL is also comprised of one barrel and two end-cap sectors. The sensors in the barrel of the HCAL are tiles of scintillating plastic whereas LAr is employed for the end-cap. A forward region, the closest possible to the beam, is covered by a LAr forward calorimeter (FCal). The LAr and Tile Calorimeter will be briefly discussed in the

539 following paragraphs.

## 540 The Liquid Argon Calorimeters

541 The ECAL is comprised of multiple layers of liquid Argon (LAr) sampler and lead ab-  
 542 sorber. The choice of its accordion-geometry design brought two main advantages; full  
 543  $\phi$  coverage with no non-interactive regions (no cracks); fast extraction of signals coming  
 544 from both front or rear end of the electrodes. It is made of two half-barrel wheels, both  
 545 placed in the barrel cryostat, that provide a pseudorapidity coverage up to  $|\eta| < 1.475$   
 546 and two end-cap detectors providing  $1.375 \leq |\eta| \leq 3.20$  coverage in two end-cap cryo-  
 547 stats. The junction between the barrel and end cap components defines the crack region  
 548 and any signal coming from the crack region is therefore discarded.

549 In the  $|\eta| < 1.8$  region there is an additional layer, placed at the front of the calorimeter,  
 550 that is made of a thin (0.5 cm in the end-cap and 1.1 cm in the barrel) LAr layer with  
 551 no absorber [25]. This additional layer was designed to correct for the energy lost, as  
 552 particles enter the calorimeter, by taking a measurement just before the majority of the  
 553 electromagnetic shower is developed.

## 554 The Tile calorimeter

555 The main purpose of the hadronic calorimeter is to measure the energy of hadronic showers.  
 556 It is built employing steel and scintillating tiles coupled to optical fibres which are read  
 557 out by photo-multipliers. As shown in Figure 2.5, the HCAL is made up of three cylin-  
 558 ders; a central barrel, 5.64 m long covering a region  $|\eta| < 1.0$ , and two extended barrel,  
 559 2.91 m long covering a reigon  $0.8 < |\eta| < 1.7$ . Each cylinder is made up of 64 modules  
 560 and each module is in turn made up of three layers. Ultimately, the smallest section of the  
 561 calorimeter module is a cell with a  $\Delta\phi \times \Delta\eta = 0.1 \times 0.1$  granularity for the two innermost  
 562 layers and  $\Delta\phi \times \Delta\eta = 0.2 \times 0.1$  for the outermost one.

### 563 2.2.4 The Muon Spectrometer

564 The MS [26], shown in Figure 2.6, is the outermost sub-system of the whole ATLAS de-  
 565 tector. As such, it surrounds the calorimeters and its main function is to perform precision  
 566 measurement of muons momenta. The deflection of muon tracks employing large super-  
 567 conducting air-core toroid magnets and high-precision tracking chambers is at the heart  
 568 of such high precision measurement.

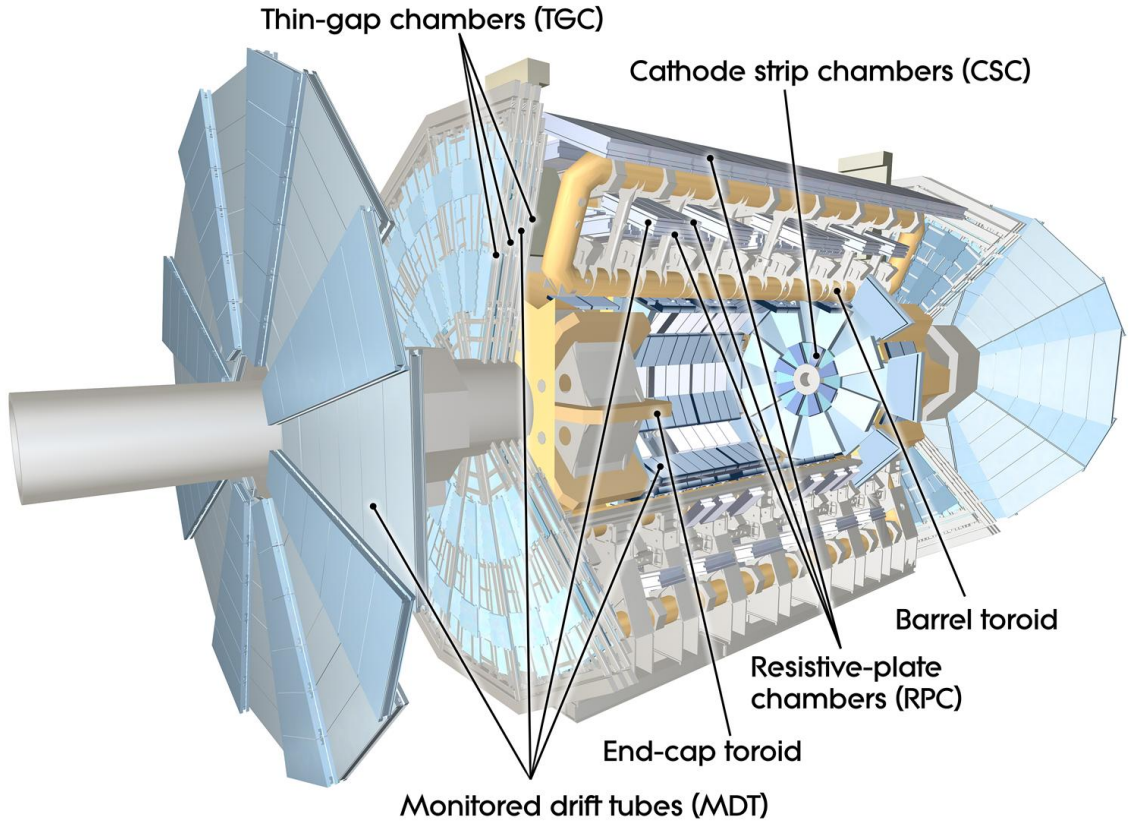


Figure 2.6: Cut-away view of the ATLAS muon system [3].

569        The MS is comprised of one large barrel toroid, covering the region  $|\eta| \leq 1.4$ , and  
 570        two end-cap toroids, covering  $1.6 < |\eta| \leq 2.7$  which are employed together to achieve the  
 571        track-bending effect wanted. The magnitude of the magnetic field in the barrel, generated  
 572        by eight large superconducting coils, ranges from 0.5 to 2 T.

573        Around the beam axis, three cylindrical layers make way for the chambers, placed in  
 574        planes perpendicular to the beam, used to measure tracks.

575        Monitored Drift Chambers (MDTs) are employed over most of the pseudorapidity  
 576        range to provide precision measurement of track coordinates in the bending direction.  
 577        Cathode Strip Chambers (CSCs) are instead employed at large pseudorapidity ( $2 < |\eta| <$   
 578        2.7). Finally, in the end-cap regions Thin-Gap Chambers (TGCs) together with Resistive-  
 579        Plate Chambers (RPCs) are dedicated to the Trigger System discussed in Section 2.3.

## 580 2.3 The ATLAS Trigger System

581        The ATLAS Trigger System is at the heart of data taking. It is an essential component of  
 582        any nuclear or particle physics experiment since it is responsible for deciding whether or  
 583        not to store an event for later study [4]. The ATLAS Trigger system is employed to reduce

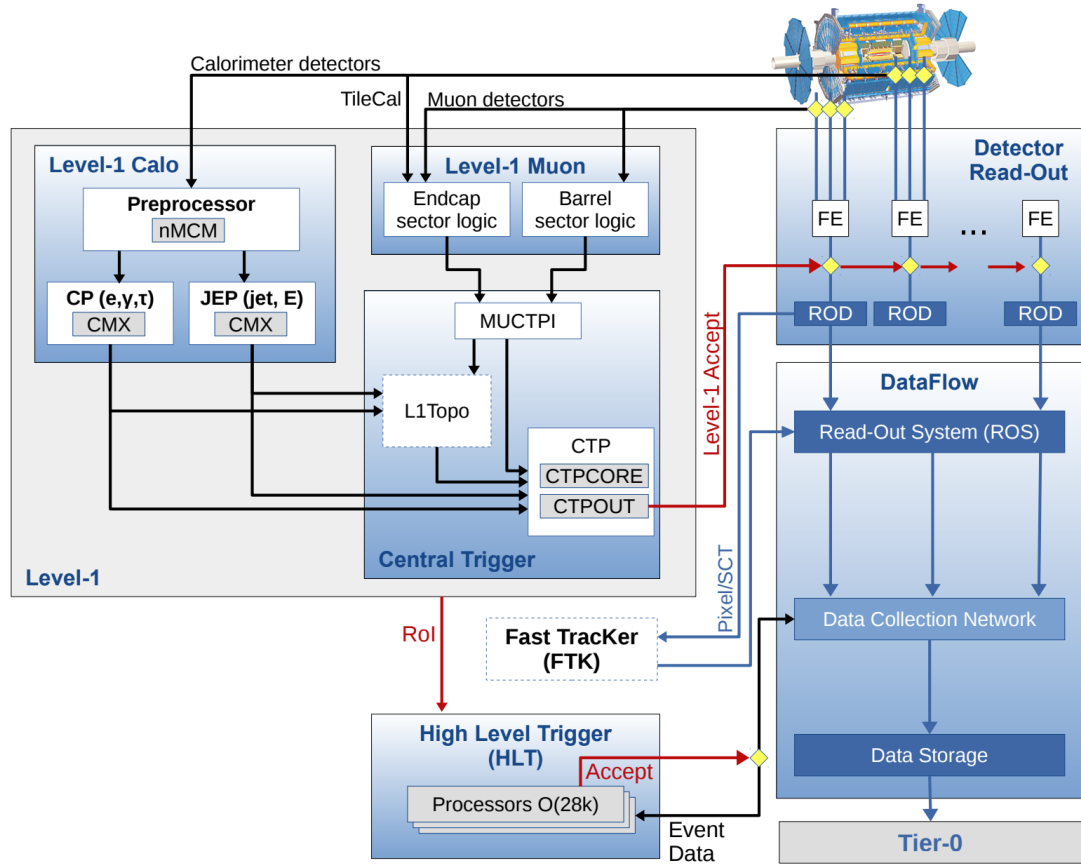


Figure 2.7: The ATLAS TDAQ system. L1Topo and FTK were being commissioned during 2015 and not used for the results shown in this thesis [4].

584 the event rate from  $\sim 40 \text{ MHz}$ <sup>1</sup> bunch-crossing<sup>2</sup> to  $\sim 200 \text{ Hz}$  which corresponds to roughly  
 585 300 MB/s.

586 The Trigger and Data Acquisition (TDAQ) system shown in Figure 2.7 consists of a  
 587 hardware-based first level trigger (L1) and a software-based high-level trigger (HLT). The  
 588 L1 trigger decision is formed by the Central Trigger Processor (CTP), which receives in-  
 589 puts from the L1 calorimeter (L1Calo) and L1 muon (L1Muon) triggers. The first level  
 590 (L1), which was designed to perform the first selection step, is a hardware-based system  
 591 that uses information from the calorimeter and muon subdetectors. It also defines the  
 592 so-called Regions of Interest (RoIs) within the detector to be investigated by the next level  
 593 trigger, the HLT. Additionally, a Fast TracKer (FTK) system [27] (not yet installed) will  
 594 provide global ID track reconstruction at the L1 trigger rate using lookup tables stored in

<sup>1</sup>The LHC delivers beams with a bunch-spacing of 25 ns.

<sup>2</sup>The term bunch-crossing is hereby used when referring to a collision between two bunches of protons. Since only a certain fraction of the total momentum carried by each proton contributes to the collision, an average number of interactions per bunch-crossing,  $\langle \mu \rangle$  is used.

595 custom associative memory chips for the pattern recognition. The FPGA-based track fitter  
 596 will perform a fast linear fit and the tracks are made available to the HLT. This system will  
 597 allow the use of tracks at much higher event rates in the HLT than is currently affordable  
 598 using CPU systems. However, the upgrade of the ATLAS trigger will not be discussed  
 599 any further.

600 In the next sections the L1 and HLT will be briefly described.

### 601 2.3.1 Level 1 Trigger

602 The Level 1 Trigger identifies Regions of Interest (RoIs)<sup>3</sup> and passes these to HLT which  
 603 will perform further investigations. Furthermore, in order to decide whether or not the  
 604 event processing will continue, L1 selection uses only information coming from some  
 605 parts of the detector to keep the input rate to a maximum of 100 kHz. L1 is implemented  
 606 in fast custom electronics to keep the latency<sup>4</sup> below 2.5  $\mu$ s. Event data from other sub-  
 607 syststem are temporarily stored in memories whilst L1 decision is taken.

608 The L1 topological trigger (L1-Topo) [28] is feeded with energy and direction inform-  
 609 ation, about the objects found by the L1 calorimeter and the muon trigger, which will be  
 610 processed by dedicated algorithms implemented in its own FPGAs. However, due to the  
 611 100 kHz read-out rate, not all the information collected by L1-Topo will be sent to the HLT,  
 612 but only part of it. In order to properly seed the ROI-guided HLT reconstruction, specific  
 613 objects in combination with the correct topological criteria must be employed.

### 614 2.3.2 High-Level Trigger

615 The HLT is used to reduce the output rate down to 1 kHz and it has a  $\sim$ 200 ms average  
 616 decision time. Events that pass L1 trigger are then processed by the HLT using finer-  
 617 granularity calorimeter information, precision measurements from the MS and tracking  
 618 information from the ID. The HLT reconstruction can be run within RoIs identified at L1  
 619 or a so-called full-scan on the full detector can be performed. The track reconstruction in  
 620 the Inner Detector is an essential component of the trigger decision in the HLT and it will  
 621 be discussed more in detail in Chapter 3

---

<sup>3</sup> $\eta - \phi$  regions where event features have been found by the L1 selection process.

<sup>4</sup>Time needed by an electric signal to get to the front-end electronics.

622 **3** | The *b*-jet Trigger Signature in AT-  
623 LAS

624 In this chapter the monitor and performance of the bottom-quark-initiated jet (*b*-jet) sig-  
625 nature trigger, this being the author’s “technical/qualification task” to become a qualified  
626 member of the experiment, will be discussed. The efficiencies of some of the Run 2 *b*-jet  
627 triggers were evaluated using  $3.8 \text{ fb}^{-1}$  of  $pp$  collisions data collected in 2015 with 25 ns  
628 bunch-spacing.

629 The qualification task

630 **3.1 Trigger Efficiency**

# 631 4 | Event Simulation and Reconstruc- 632 tion

633 bla bla bla

## 634 4.1 Event Generation

635 bla bla

### 636 4.1.1 Parton Distribution Functions (PDFs)

637 bla bla bla

### 638 4.1.2 Matrix Element Calculation

639 bla bla bla

### 640 4.1.3 Parton Showers

641 bla bla bla

### 642 4.1.4 Hadronisation

643 bla bla bla

## 644 4.2 Detector Simulation

645 bla bla bla

646

**5**

647

648

## Stop searches in final states with jets and missing transverse energy

649 6

650

## Results and Statistical Interpretations

651 Trigger

652 bla vlas bla

# Bibliography

- [1] ATLAS Collaboration, "Summary plots from the atlas standard model physics group." [https://atlas.web.cern.ch/Atlas/GROUPS/PHYSICS/CombinedSummaryPlots/SM/ATLAS\\_a\\_SMSummary\\_TotalXsect/ATLAS\\_a\\_SMSummary\\_TotalXsect.png](https://atlas.web.cern.ch/Atlas/GROUPS/PHYSICS/CombinedSummaryPlots/SM/ATLAS_a_SMSummary_TotalXsect/ATLAS_a_SMSummary_TotalXsect.png). viii, 9
- [2] C. Lefèvre, *The CERN accelerator complex.*, <http://cds.cern.ch/record/1260465>. viii, 15, 16
- [3] ATLAS Collaboration, *The ATLAS experiment at the CERN Large Hadron Collider*, Journal of Instrumentation **3** no. 08, (2008) S08003. <http://stacks.iop.org/1748-0221/3/i=08/a=S08003>. viii, 17, 23
- [4] A. Collaboration, *Performance of the ATLAS Trigger System in 2015*, Eur. Phys. J. **C77** (2017), [arXiv:1611.09661 \[hep-ex\]](arXiv:1611.09661). viii, 23, 24
- [5] M. Herrero, *The Standard Model.*, <https://arxiv.org/abs/hep-ph/9812242>. 3
- [6] ATLAS Collaboration, *Observation of a New Particle in the Search for the Standard Model Higgs Boson with the ATLAS Detector at the LHC*, Phys.Lett. **B716** (2012), [arXiv:1207.7214 \[hep-ex\]](arXiv:1207.7214). 3
- [7] CMS Collaboration, *Observation of a new boson at a mass of 125 GeV with the CMS experiment at the LHC*, Phys.Lett. **B716** (2012), [arXiv:1207.7235 \[hep-ex\]](arXiv:1207.7235). 3
- [8] A. Pich, *The Standard Model of Electroweak Interactions*, [arXiv:1201.0537 \[hep-ph\]](arXiv:1201.0537). 5, 6
- [9] K. A. Olive at al. (Particle Data Group), *Review of Particle Physics*, Chin.Phys. C **38(9)** (2014). 6
- [10] J. Goldstone, A. Salam and S. Weinberg, *Broken Symmetries*, Phys. Rev. **127** (1962) 965–970. 8

- 677 [11] S. Weinberg, *Implications of Dynamical Symmetry Breaking*, Phys. Rev. **D19** (1976)  
 678        1277–1280. 10
- 679 [12] Super-Kamiokande Collaboration, Y. Fukuda et al., *Evidence for oscillation of*  
 680        *atmospheric neutrinos*, Phys. Rev. Lett. **81** (1998) 1562–1567, arXiv:hep-ex/9807003  
 681        [hep-ex]. 10
- 682 [13] SNO Collaboration, *Measurement of the Rate of  $\nu_e + d \rightarrow p + p + e^-$  Interactions*  
 683        *Produced by  $^8B$  Solar Neutrinos at the Sudbury Neutrino Observatory*, Phys. Rev. Lett.  
 684        **87** (2001). 10
- 685 [14] T. O. W. of the Nobel Prize.  
 686        [https://www.nobelprize.org/nobel\\_prizes/physics/laureates/2015/](https://www.nobelprize.org/nobel_prizes/physics/laureates/2015/). 10
- 687 [15] J.M. Jowett, M. Schaumann, R. Alemany, R. Bruce, M. Giovannozzi, P. Hermes, W.  
 688        Hofle, M. Lamont, T. Mertens, S. Redaelli, J. Uythoven, J. Wenninger, *The 2015*  
 689        *Heavy-Ion Run of the LHC*,  
 690        <http://accelconf.web.cern.ch/accelconf/ipac2016/papers/tupmw027.pdf>. 14
- 691 [16] O. S. Brüuning, P. Collier, P. Lebrun, S. Myers, R. Ostojic, J. Poole and P. Proudlock,  
 692        *LHC Design Report*, <https://cds.cern.ch/record/782076>. 15
- 693 [17] CMS Collaboration, *The CMS experiment at the CERN LHC*, Journal of  
 694        Instrumentation **3** no. 08, (2008) S08004.  
 695        <http://stacks.iop.org/1748-0221/3/i=08/a=S08004>. 15
- 696 [18] LHCb Collaboration, et. al, *The LHCb Detector at the LHC*, JINST (2008). 15
- 697 [19] ALICE Collaboration, *The ALICE experiment at the CERN LHC*, Journal of  
 698        Instrumentation **3** no. 08, (2008) S08002.  
 699        <http://stacks.iop.org/1748-0221/3/i=08/a=S08002>. 15
- 700 [20] A. Yamamoto, Y. Makida, R. Ruber, Y. Doi, T. Haruyama, F. Haug, H. ten Kate,  
 701        M. Kawai, T. Kondo, Y. Kondo, J. Metselaar, S. Mizumaki, G. Olesen, O. Pavlov,  
 702        S. Ravat, E. Sbrissa, K. Tanaka, T. Taylor, and H. Yamaoka, *The ATLAS central*  
 703        *solenoid*, Nuclear Instruments and Methods in Physics Research Section A:  
 704        Accelerators, Spectrometers, Detectors and Associated Equipment **584** no. 1, (2008)  
 705        53 – 74.  
 706        <http://www.sciencedirect.com/science/article/pii/S0168900207020414>. 17,  
 707        18

- 708 [21] ATLAS Collaboration, *The ATLAS Inner Detector commissioning and calibration*, Eur.  
709 Phys. JC70 , arXiv:1004.5293. 18
- 710 [22] ATLAS Collaboration, *ATLAS Insertable B-Layer Technical Design Report.*,  
711 <https://cds.cern.ch/record/1291633>. 19
- 712 [23] G. A. et al., *ATLAS pixel detector electronics and sensors*, Journal of Instrumentation 3  
713 no. 07, (2008) P07007. <http://stacks.iop.org/1748-0221/3/i=07/a=P07007>. 20
- 714 [24] A. Bingül, *The ATLAS TRT and its Performance at LHC*, Journal of Physics:  
715 Conference Series 347 no. 1, (2012) 012025.  
716 <http://iopscience.iop.org/article/10.1088/1742-6596/347/1/012025/meta>.  
717 20
- 718 [25] ATLAS Collaboration, *ATLAS liquid-argon calorimeter: Technical Design Report.*,  
719 <https://cds.cern.ch/record/331061>. 22
- 720 [26] ATLAS Collaboration, *ATLAS muon spectrometer: Technical design report.*,  
721 <https://cds.cern.ch/record/331068>. 22
- 722 [27] ATLAS Collaboration, *Fast TracKer (FTK) Technical Design Report.*,  
723 <https://cds.cern.ch/record/1552953>. 24
- 724 [28] E. Simoni, *The Topological Processor for the future ATLAS Level-1 Trigger: from design to  
725 commissioning*, arXiv:1406.4316. 25